Bio-Design and Manufacturing (2026) 9:399–414
https://doi.org/10.1631/bdm.2500276

RESEARCH ARTICLE

# Diatom-derived magnetic biohybrid microrobots for photodynamic therapy in glioblastoma

Mengyue Li[1,2] · Wen Cheng[4] · Xuechun Wang[4] · Junjian Zhou[2,3] · Yuting Zhou[2,3] · Tianyang Ma[4] · Anhua Wu[4] · Lianqing Liu[2] · Niandong Jiao[2]

Received: 26 May 2025 / Accepted: 20 September 2025 / Published online: 16 February 2026


**Abstract**

Diatoms, as natural sources of porous silica, have important potential for biomedical applications. Biohybrid microrobots also show promise for targeted delivery; however, research on converting diatoms into biohybrid microrobots and exploiting their intrinsic properties for cancer treatment remains limited. In this study, *Thalassiosira weissflogii* was transformed into biohybrid microrobots (Mag-Diatoms) while retaining its natural chlorophyll, thereby enabling Mag-Diatom-mediated photodynamic therapy (PDT) without additional drug modification. In this system, Mag-Diatoms acted as microrobots, and their intrinsic chlorophyll served as a photosensitizer, exhibiting excellent biological safety. The autonomous closed-loop motion of the Mag-Diatoms was achieved using an artificial intelligence algorithm, which enabled controlled navigation along a preset trajectory. Mag-Diatoms also exhibited the ability to traverse narrow slits and target cancer cells within a cellular environment. The PDT effect was validated in vitro using human malignant glioblastoma (GBM) cell lines and primary cells derived from patients. The results revealed that the cell viability was closely related to the Mag-Diatom concentration, laser intensity, and irradiation time. Under combined Mag-Diatoms and laser treatment, viability decreased to 19.5% in primary cells and 3.6% in cell line models. Moreover, in vivo experiments using a mouse glioma model revealed that Mag-Diatom-mediated PDT effectively suppressed GBM progression. These findings highlight the potential of diatom-derived biohybrid microrobots, leveraging their natural properties, as a novel material and solution for PDT-based GBM therapy.

Mengyue Li, Wen Cheng, and Xuechun Wang have contributed equally to this work.

✉ Anhua Wu
ahwu@cmu.edu.cn

✉ Lianqing Liu
lqliu@sia.cn

✉ Niandong Jiao
ndjiao@sia.cn

[1] School of Computer Science, South-Central Minzu University, Wuhan 430074, China

[2] State Key Laboratory of Robotics and Intelligent Systems, Shenyang Institute of Automation, Chinese Academy of Sciences, Shenyang 110016, China

[3] University of Chinese Academy of Sciences, Beijing 100049, China

[4] Department of Neurosurgery, Shengjing Hospital of China Medical University, Shenyang 110022, China

**Graphical abstract**

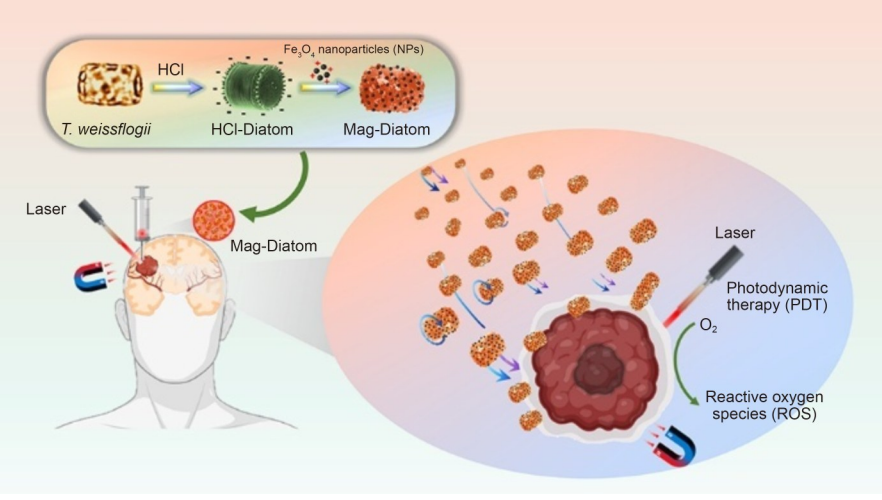


**Keywords** Diatom · Biohybrid microrobots · Autonomous movement · Photodynamic therapy · Glioblastoma

## 1 Introduction

Micro- and nanorobots can access difficult-to-reach areas of the human body due to their small size and flexible mobility. They have demonstrated a wide range of potential applications in targeted delivery, medical diagnostics, and surgical therapy in recent years [1–9]. These devices convert external chemical or physical energy into kinetic energy, enabling diverse modes of locomotion. Rapid progress has been made in the development of micro- and nanorobots with multiple motion mechanisms, and many efforts have been directed toward their biomedical application [10–14]. Biohybrid micro- and nanorobots integrate biological components—such as living cells, enzymes, and biomembranes—with artificial structures to achieve autonomous motion and carry out specific functions [15–18]. Their design leverages the inherent properties of biological elements, such as self-healing, biosensing, actuation, and unique structural and compositional features. These properties can be further modified or engineered to meet specific application requirements, thereby improving their potential. Biohybrid micro- and nanorobots offer excellent biocompatibility and exhibit improved adaptability to complex microenvironments. They hold promise for applications in targeted delivery, biosensing, and cancer therapy [19–22]. Continued research aims to optimize the functional characteristics of biomaterials and to improve the mobility and therapeutic potential of biohybrid micro- and nanorobots, reinforcing their value as emerging tools in biomedicine.

Targeted delivery technologies can enhance diagnostic and therapeutic outcomes while minimizing adverse effects, making them a promising approach in biomedical applications [5, 23]. However, drug leakage remains a major challenge in delivery systems. Because of their distinct morphological properties—such as their easily adjustable size and shape, high dispersibility, stability, and ease of surface modification—mesoporous silica particles are frequently used in drug delivery [24]. Compared with traditional nanocarriers, mesoporous silica offers distinct advantages as a drug delivery system [25–27]. However, its synthesis often requires toxic reagents, such as silane and hydrofluoric acid, and the preparation process is complex, time-consuming, and expensive. In comparison, diatoms—naturally occurring silica-based materials—represent a more environmentally friendly and economical alternative owing to their complex porous structure and diverse morphologies [28, 29]. Diatoms are single-celled photosynthetic algae that contribute to an estimated 20% of global oxygen production annually. Their silica-based cell walls are layered and three-dimensional, providing mechanical stability, high surface area, and broad potential in the biomedical field [30]. Previous studies have explored the application of diatoms in targeted delivery, bone regeneration, hemostasis, and signal detection [31–33], and their conversion into microrobots for biomedical applications has also been studied [34–37]. *Thalassiosira weissflogii* (*T. weissflogii*) is a unicellular marine diatom widely distributed across oceanic environments. It belongs to the genus *Thalassiosira*, within the order Centrales. The cells are typically circular or oval, with diameters ranging from 10 to 20 μm. Their intricately patterned siliceous frustule provides high mechanical strength and exceptional chemical stability. Due to these properties,

*T. weissflogii* has been extensively investigated as a platform for drug delivery and biosensing applications [38]. The silica frustule surface can be functionalized with various chemical moieties, such as therapeutic agents and nanoparticles, enabling targeted delivery and enhancing the therapeutic efficacy [39, 40]. However, the intrinsic biological components of diatoms, such as chlorophyll, remain underexplored for biomedical use. The unique structural and functional properties of diatoms represent a valuable resource for future research and hold potential to drive further innovation in the biomedical field.

Glioblastoma (GBM) is the most common and aggressive primary malignant tumor of the central nervous system [41, 42]. According to the WHO CNS5 classification, GBM is defined as an isocitrate dehydrogenase (IDH)-wildtype diffuse glioma with distinct molecular features; other gliomas include astrocytoma, IDH-mutant, and oligodendroglioma, IDH-mutant and 1p/19q-codeleted [42]. Multimodal therapy—consisting of maximal safe surgical resection, radiotherapy, and temozolomide chemotherapy—remains the standard of care. However, the highly invasive and infiltrative nature of GBM precludes complete eradication. Consequently, despite comprehensive treatment [43], patients almost inevitably face tumor recurrence and ultimately death [44, 45]. Furthermore, profound intratumoral heterogeneity, therapeutic resistance, and the absence of effective targeted therapies continue to represent major challenges in GBM management [42]. Photodynamic therapy (PDT) has emerged as a potential therapeutic option for GBM. PDT relies on photosensitizers that, when activated by light of a specific wavelength, generate reactive oxygen species (ROS) capable of destroying tumor cells [46]. This approach is spatially and temporally selective, enabling targeted cytotoxicity against cancer cells while producing relatively low systemic toxicity to normal tissues. PDT has shown promise in preclinical and clinical studies for GBM and is increasingly considered an attractive adjunct therapy [47, 48]. The clinical efficacy of photosensitizers is limited by three key factors: restricted penetration of the blood–brain barrier, selective accumulation in tumor tissue, and the need for activation by long-wavelength light suitable for deep tissue. First-generation photosensitizers (e.g., Photofrin® and hematoporphyrin derivative (HpD)) were the earliest used clinically but were hampered by poor tumor selectivity and severe phototoxicity [48, 49]. Second-generation photosensitizers (e.g., meta-tetrahydroxyphenylchlorin (mTHPC) and 5-aminolevulinic acid (5-ALA)) offered improved photophysical properties and tumor targeting [50]; among them, 5-ALA has been applied in intraoperative navigation and PDT for GBM. However, their use is still constrained by limited blood–brain barrier penetration and uncontrolled drug release [51, 52]. Third-generation photosensitizers, typically combined with nanocarriers, enhance cellular uptake and drug release regulation. These platforms incorporate features such as oxygen supply, hypoxia-activated mechanisms, and multidrug combination delivery [53–56]. However, issues related to drug targeting, in vivo stability, and real-time monitoring remain unresolved [57]. Fabricating diatoms into microrobots and exploiting their intrinsic chlorophyll as a photosensitizer may overcome some of these limitations. This approach eliminates the need for exogenous drug loading and reduces the risk of leakage. Moreover, the robust porous silica framework of diatoms, combined with magnetic navigation, offers a promising strategy for efficient and safe PDT in GBM.

In this study, we developed a diatom-based biohybrid magnetic microrobot, termed Mag-Diatom, for PDT of GBMs (Fig. 1). Chlorophyll in algae has previously been studied as a photosensitizer for PDT [58, 59], and diatoms naturally contain chlorophyll [60]. Therefore, Mag-Diatom does not require additional drug-loading modifications. Instead, it uses the intrinsic chlorophyll in diatoms as a photosensitizer to achieve in situ PDT, thereby providing a novel platform for GBM therapy. The fabricated Mag-Diatoms showed efficient mobility, with closed-loop trajectory tracking achieved through simple proportional–integral–differential (PID) control. They also exhibited the ability to autonomously change movement modes and traverse narrow channels. In addition, combined with artificial intelligence (AI) algorithms, the ability of Mag-Diatoms to autonomously track movement trajectories and precisely deliver to target cells was proven. The dual movement modes improved environmental adaptability, whereas the integration of AI algorithms enhanced autonomous and flexible movement control. Human malignant glioblastoma cells (U87), primary glioma cells (GSC63), and mouse glioma models were used to verify the photodynamic capabilities of the prepared Mag-Diatom. Experimental results indicated that Mag-Diatoms effectively induced PDT, exhibiting promise as a biohybrid therapeutic platform for GBM. Notably, their reliance on endogenous chlorophyll simplified the material preparation process and mitigated the risk of drug leakage associated with conventional delivery systems. By leveraging the natural properties of diatoms and integrating AI-based control, Mag-Diatom represents a potentially efficient and safe treatment tool for GBM treatment.

## 2 Materials and methods

### 2.1 Instrument and analyses

A Quattro S instrument (Thermo Fisher Scientific, USA) was used to obtain energy-dispersive spectrometer (EDS) mapping and scanning electron microscopy (SEM) images. Dynamic light scattering measurements were performed

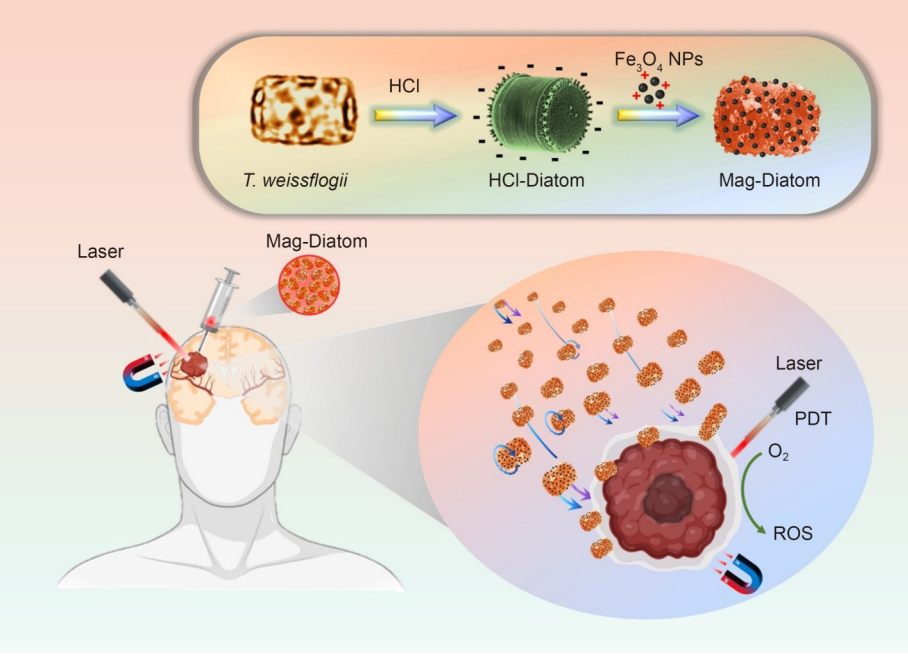


**Fig. 1** Schematic illustration of Mag-Diatom-mediated PDT

using a Zetasizer Nano ZSP (Malvern, UK) to determine the zeta potential. The magnetic properties of Mag-Diatoms and $Fe_3O_4$ nanoparticles (NPs) were analyzed using a Lake Shore 740 vibrating sample magnetometer (Lake Shore, USA). A Ti2-E inverted fluorescence microscope (Nikon, Japan) was used to take both brightfield and fluorescence images. An ultraviolet–visible–near-infrared (UV–Vis–NIR) spectrometer (Lambda 1050+, PerkinElmer, USA) was used to obtain absorption spectra. Fluorescence imaging was performed at specific wavelengths using a CrestOptics X-Light V3 spinning disk confocal microscope (Nikon). A DNM-9602G microplate reader (Perlong Medical, China) was used to perform the cell counting kit-8 (CCK-8) assays. Slit structures were fabricated through three-dimensional (3D) microprinting using a commercial two-photon polymerization system (Photonic Professional GT2, Nanoscribe GmbH, Germany).

## 2.2 Cultivation of diatoms and preparation of Mag-Diatoms

*T. weissflogii* was obtained from Shanghai Guangyu Biotechnology Co., Ltd. (China). The diatom cells were cultured in an incubator (GZP-150BE, LICHEN, China) under a 12:12-h light–dark cycle at 24 °C, with light intensity set to 2000 lx. The cultures were concentrated by centrifugation at 2000*g* for 5 min to yield a final cell density of $5\times10^6$ cells/mL. Following a 4-h dark treatment with 0.1 mol/L hydrochloric acid, the diatom cells were washed twice by centrifugation with deionized water. To prepare Mag-Diatoms, 300 μg of $Fe_3O_4$ NPs was mixed with 1 mL of diatom cell suspension (1 mg/mL) and shaken for 1.5 h.

## 2.3 Magnetic control of Mag-Diatoms

The movement of Mag-Diatoms was regulated using a five-coil magnetic system integrated into an inverted microscope. The system consisted of four mutually perpendicular iron-core coils arranged in the horizontal plane and one non-iron-core coil positioned in the vertical plane. The effective circular working area of the system was 40 mm in diameter. A desired output signal was generated in LabVIEW and transmitted through an input/output card (NI PCIe-6738) to a servo amplifier (Maxon ESCON 50/5). The amplifier then transmitted the signal to the five electromagnetic coils, which in turn produced the required magnetic fields.

## 2.4 Cell culture

Commercially available U87 cells were cultivated in Dulbecco's modified Eagle's medium (DMEM) supplemented with 200 nmol/L L-glutamine, 10% fetal bovine serum, and 1% penicillin-streptomycin at 37 °C and 5% $CO_2$. Primary GBM cells (GSC63) were isolated from recently excised GBM tissue obtained from a patient at the First Affiliated Hospital of China Medical University. Sleeping Beauty (SB) mouse glioma sphere cells (mGSCs) were derived from a de novo-induced spontaneous GBM model based on a previously reported murine spontaneous glioma model [61]. GSC63 and SB mGSCs were maintained in stem cell medium

consisting of DMEM/F12 supplemented with 2% B27, 10 ng/mL epidermal growth factor, and 10 ng/mL fibroblast growth factor.

## 2.5 In vitro cell experiments

Cell viability was assessed using the standard CCK-8 cell assay. U87 cells were seeded in 96-well plates at a density of 6000 cells/well. After 24 h of culture, diatoms and Mag-Diatoms were added at various concentrations ($0.625\times10^4$, $1.25\times10^4$, $1.875\times10^4$, $2.5\times10^4$, $18.75\times10^4$, $25\times10^4$, $62.5\times10^4$, and $125\times10^4$ cells/mL). After 24 and 48 h of culture, the cells were washed twice with phosphate-buffered saline (PBS), and the culture medium containing 10 μL of the CCK-8 reagent was added. Absorbance at 450 nm was measured using a microplate reader (DNM-9602 G, Perlong Medical). These experiments were used to assess the biocompatibility of diatoms and Mag-Diatoms with U87 cells. To evaluate PDT effects, U87 cells were treated with Mag-Diatoms at concentrations of $6\times10^4$, $8\times10^4$, $10\times10^4$, and $12\times10^4$ cells/mL. After 5 h of culture, the cells were irradiated with a 638-nm laser (43.5 mW) for 2 min, and then cultured for an additional 12 h. The cells were washed twice with PBS, CCK-8 reagent was added, and the absorbance was measured after 1 h. Further experiments were conducted to examine the influence of laser intensity and irradiation time. U87 cells with or without Mag-Diatoms (120 000 cells/mL) after 5 h of culture were irradiated either at different intensities (0, 14.1, 28.0, and 43.5 mW for 2 min) or at 43.5 mW laser power for varying durations (0, 2, 5, and 10 min). The cells were then cultured for 12 h, washed twice with PBS, and treated with CCK-8 reagent; the absorbance of each well was measured following a 1-h incubation.

Primary GSC63 cells were seeded in 96-well plates at 20 000 cells/well and cultivated for 24 h. Mag-Diatoms (0, 8000, 10 000, and 12 000) were then added to each well and cultured for 5 h. The cells were irradiated with a 638-nm laser (43.5 mW) for 5 min, cultured for 12 h, and treated with CCK-8 reagent; the absorbance was measured after 3 h. To further evaluate PDT effects, GSC63 cells were treated with or without 12 000 Mag-Diatoms, cultured for 5 h, and exposed to laser irradiation at different intensities (0, 14.1, 28.0, and 43.5 mW for 5 min). After 12 h of culture, the CCK-8 reagent was added, and the absorbance was measured after 3 h. In another set of experiments, 10 000 Mag-Diatoms were either added to or omitted from 96-well plates with primary GSC63 cells and irradiated with a 43.5-mW laser for 0, 2, 5, or 10 min following 5 h of incubation. After an additional 12 h, CCK-8 reagent was added, and the absorbance was measured 3 h later.

## 2.6 Construction and treatment of tumor models

Mice were housed in ventilated cages in groups, under controlled humidity and temperature with a 12-h light–dark cycle. Prior to the experiments, each animal was randomly assigned a body weight. For the orthotopic mouse model, 5-week-old male C57 mice (Beijing HFK BioScience Co., Ltd., China) were implanted with SB mGSCs ($2\times10^5$ cells per mouse) through stereotactic intracranial injection to establish an SB-bearing murine model. The injection coordinates were 2.0 mm posterior to the anterior fontanelle, 2.0 mm lateral to the midline, and 2.0 mm in depth.

Two weeks after orthotopic tumor implantation, mice exhibited remarkable neurological symptoms, and successful glioma establishment was confirmed through in vivo imaging (NightOWL II LB983, Berthold Technologies, Germany). Mice were then randomized into four groups ($n$= 3 per group): Control, Laser (638 nm, 5 min of irradiation on Days 15 and 17), Mag-Diatom (25 000 units intracranially on Day 15), and Mag-Diatom+Laser (combined treatment as above). On Day 15, mice in the Mag-Diatoms groups received an intracranial injection of 1 μL of Mag-Diatoms (25 000 units), followed by localized 638-nm laser irradiation (5 min) for the laser-treated groups. A second irradiation was performed on Day 17. The final in vivo imaging session was performed on Day 21, after which mice were euthanized with carbon dioxide. Body weight changes were recorded throughout the experiment, and data were analyzed using GraphPad PRISM software.

## 2.7 Statistical analysis

Data are presented as mean±standard deviation. Origin 10.1.0 (Learning Version) (Origin Lab, USA) was used for statistical analysis. Each experiment was conducted in at least three independent replicates. Statistical significance was evaluated using Student's $t$-test. Significance values were defined as $^{*}p<0.05$, $^{**}p<0.01$, $^{***}p<0.001$, and $^{****}p<0.0001$.

# 3 Results and discussion

## 3.1 Preparation and characterization of Mag-Diatoms

### 3.1.1 Diatom cell pretreatment

*T. weissflogii* was selected as the biological template for preparing Mag-Diatoms. Figure 2a shows a bright-field image of the cylindrical *T. weissflogii* cells. The diatom cells were initially treated with hydrochloric acid (HCl) to remove the calcium-based cementing compounds from their

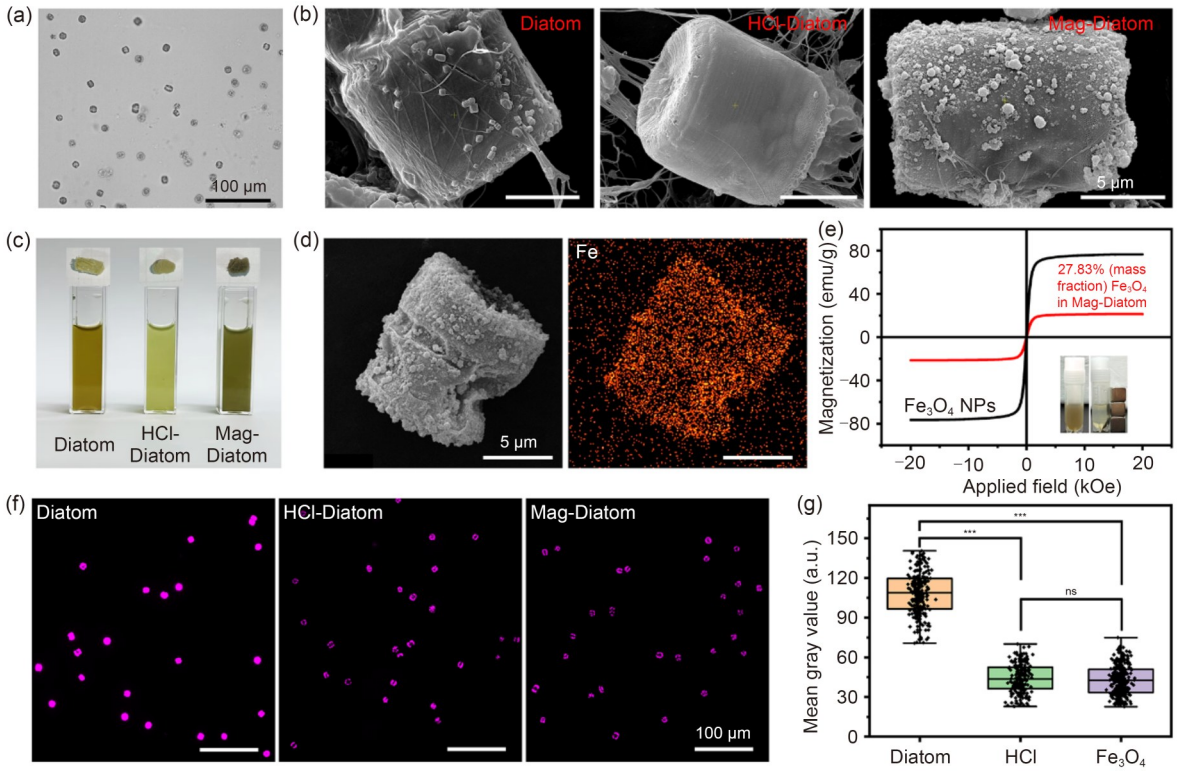


**Fig. 2** Preparation and characterization of Mag-Diatoms. (a) Bright-field image of cylindrical *T. weissflogii* cells. (b) SEM images of diatom cells, HCl-Diatoms, and Mag-Diatoms. (c) Digital images of diatom cells, HCl-Diatoms, and Mag-Diatoms in deionized water (bottom) and as freeze-dried powder (top). (d) SEM image of a Mag-Diatom with corresponding EDS mapping of Fe. (e) Magnetization curves of Mag-Diatoms and $Fe_3O_4$ NPs. (f) Fluorescence images of diatom cells, HCl-Diatoms, and Mag-Diatoms. (g) Average fluorescence intensity of diatom cells, HCl-Diatoms, and Mag-Diatoms. $^{***}p<0.001$; ns: not significant. 1 emu=$10^{-3}$ A·m$^2$; 1 Oe=1000/(4π) A/m

surfaces, yielding HCl-treated diatoms (HCl-Diatoms) with smooth, porous surfaces. To determine the optimal HCl concentrations, we evaluated the absorbance of diatom suspensions following treatment with various HCl concentrations, as well as the magnetic response of the subsequently modified $Fe_3O_4$ NPs (Fig. S1 in the supplementary information). Absorbance served as an indicator of chlorophyll content in the suspension, and the magnetic response reflected the motility characteristics of Mag-Diatoms. Although 0.1 mol/L HCl produced a slightly weaker magnetic response than 1 mol/L HCl (Fig. S1c in the supplementary information) and absorbance values were comparable (Fig. S1a in the supplementary information), the 0.1 mol/L treatment effectively removed surface impurities, reduced reagent costs, avoided corrosion from higher concentrations, and lowered potential environmental impact. Therefore, 0.1 mol/L HCl was selected as the pretreatment condition for *T. weissflogii* cells.

### 3.1.2 Preparation and characterization of Mag-Diatoms

The surface of HCl-Diatoms carried a negative charge, with a zeta potential of − 29.8 mV (Fig. S2 in the supplementary information). The zeta potential of the $Fe_3O_4$ NPs was +47.97 mV, indicating a positively charged surface (Fig. S2 in the supplementary information). Since the surface charges of the two materials were opposite, $Fe_3O_4$ NPs were coated onto the surface of HCl-Diatoms through electrostatic adsorption. The zeta potential of the Mag-Diatoms modified with $Fe_3O_4$ NPs was − 5.8 mV (Fig. S2 in the supplementary information). Figure 2b shows SEM images of diatoms at different treatment stages, with enlarged views provided in Fig. S3 (supplementary information). The SEM images revealed that the surfaces of HCl-Diatoms were cleaner than those of untreated diatom cells, and their porous structures were more distinct, which is conducive to the subsequent attachment of $Fe_3O_4$ NPs. The images also confirmed the successful deposition of $Fe_3O_4$ NPs onto the diatom surfaces, verifying that the Mag-Diatom was successfully prepared. Macroscopic images of diatom suspensions and freeze-dried samples at various treatment stages are shown in Fig. 2c. Elemental composition analyses of diatom cells, HCl-Diatoms, and Mag-Diatoms were conducted using EDS. As shown in the EDS mapping image (Fig. 2d), Fe was detected on the surfaces of the prepared Mag-Diatom, confirming the incorporation of $Fe_3O_4$. The saturation magnetization of $Fe_3O_4$ NPs was 76.61 emu/g (1 emu=$10^{-3}$ A·m$^2$), whereas that of Mag-Diatoms was 21.32 emu/g, corresponding to a $Fe_3O_4$ mass concentration

of 27.83% (Fig. 2e). The magnetization curves (Fig. 2e) further show that Mag-Diatoms possessed favorable paramagnetic properties. The inset in Fig. 2e shows that Mag-Diatoms could be separated from liquid using external magnets, indicating strong magnetic properties. Thus, these results confirm that *T. weissflogii* cells were successfully converted into Mag-Diatoms and that surface modification with $Fe_3O_4$ NPs endowed them with magnetic properties.

#### 3.1.3 Verification of chlorophyll in Mag-Diatoms

Natural diatoms contain chlorophyll [60], which emits strong fluorescence under the excitation of a Cy5-band laser [62]. Figure 2f shows confocal images of diatoms at different processing stages. Diatom cells, HCl-Diatoms, and Mag-Diatoms all emitted fluorescence when stimulated by the C640 laser channel. As shown in Fig. 2g, the fluorescence intensity of diatoms decreased after HCl treatment; however, the attachment of $Fe_3O_4$ NPs did not affect the fluorescence intensity. Moreover, the absorbance spectra of diatom cells, HCl-Diatoms, Mag-Diatoms, and $Fe_3O_4$ NP suspensions were measured using a UV–Vis–NIR spectrophotometer (Fig. S4 in the supplementary information). The results revealed that Mag-Diatoms retained the characteristic absorption peak of diatom cells at 675 nm. EDS mapping images (Fig. S5 in the supplementary information) further confirmed the presence of Mg in diatom cells, HCl-Diatoms, and Mag-Diatoms. Given that Mg is a key element of chlorophyll, these results indicate that the prepared Mag-Diatoms preserved chlorophyll from the original diatom cells. Overall, the results indicated that Mag-Diatoms retained part of the chlorophyll content and exhibited fluorescent properties.

### 3.2 Locomotion of Mag-Diatoms

The locomotion performance of biohybrid microrobots is critical for their targeted delivery. The magnetic responsiveness of Mag-Diatoms enables external control through the application of magnetic fields. Figure 3a presents a schematic diagram illustrating the movement of Mag-Diatoms in a rotating magnetic field, defined as

$$H(t) = H\left[\cos(\omega t)\boldsymbol{e}_y - \sin(\omega t)\boldsymbol{e}_z\right],$$

where $\boldsymbol{e}_y$ and $\boldsymbol{e}_z$ are unit vectors along the $y$-axis and $z$-axis, respectively, $H$ denotes the magnetic field intensity, and $\omega$ represents the frequency. Given their cylindrical shape, Mag-Diatoms exhibit two distinct motion modes under an external magnetic field [63]. By varying the magnetic field frequency while maintaining constant intensity, their motion can change from tumbling along the long axis to rolling along the short axis (Video S1 in the supplementary information). Superimposed images of these two motion modes are displayed in Fig. 3b. The velocity of Mag-Diatoms was further characterized at various magnetic field intensities and frequencies (Fig. 3c). Step-out frequency and maximum velocity increased with greater magnetic field intensity. Under a constant magnetic field intensity, the velocity initially increased but subsequently decreased. At a magnetic field intensity of 10 mT and frequency of 11 Hz, the Mag-Diatoms reached a maximum velocity of 71.24 μm/s. Overall, the prepared Mag-Diatoms exhibit efficient magnetic-field-driven locomotion, two distinct motion modes, and tunable velocities.

The closed-loop autonomous motion enhances the intelligence, stability, and flexibility of biohybrid microrobots for targeted delivery. In this study, Mag-Diatoms were controlled using a PID controller to follow preset trajectories in the shapes of a heart, a star, and a crescent moon (Video S2 in the supplementary information). The rotating magnetic field was maintained at a strength of 10 mT. Figure 3d shows the intended and actual trajectories, where the white line represents the programmed path and the yellow line represents the actual trajectory of the Mag-Diatom. Moreover, the real-time distance errors corresponding to these trajectories (Fig. S6 in the supplementary information) indicate high control accuracy, with root mean square errors of 11.93, 10.22, and 9.89 pixels (0.37 μm per pixel), respectively. The two motion modes of Mag-Diatom—movement along the long axis and the short axis—determine that the minimum slit width they can pass through is constrained by the length of the short axis. To evaluate this capacity, slits of different widths were fabricated using two-photon 3D printing. By adjusting the magnetic field frequency while maintaining a constant field strength of 10 mT, Mag-Diatoms autonomously passed through narrow channels along predetermined trajectories (Video S3 in the supplementary information). Figure 3e shows the overall movement process of the Mag-Diatom from the open area, through the slit, and back to the open area. The long axis of the controlled Mag-Diatom was 18.76 μm, the short axis was 12.22 μm, and it successfully traversed channels as narrow as 18 μm in width. In open regions, Mag-Diatoms predominantly moved along the short axis, which enabled faster locomotion and quicker arrival at target sites. When facing a narrow slit, they switched motion along the long axis, allowing them to pass more slowly but effectively through complex or confined environments. Upon re-entering an open area, they reverted to short-axis motion to continue rapid travel toward subsequent targets.

Using an algorithm developed in a previous study [64], the autonomous cell-targeting ability of Mag-Diatoms was evaluated using U87 cells. The AM-YOLOv7 algorithm was applied to identify Mag-Diatoms and U87 cells, the A* algorithm was used to plan the trajectory, and the PID controller was used to track and guide the Mag-Diatoms from

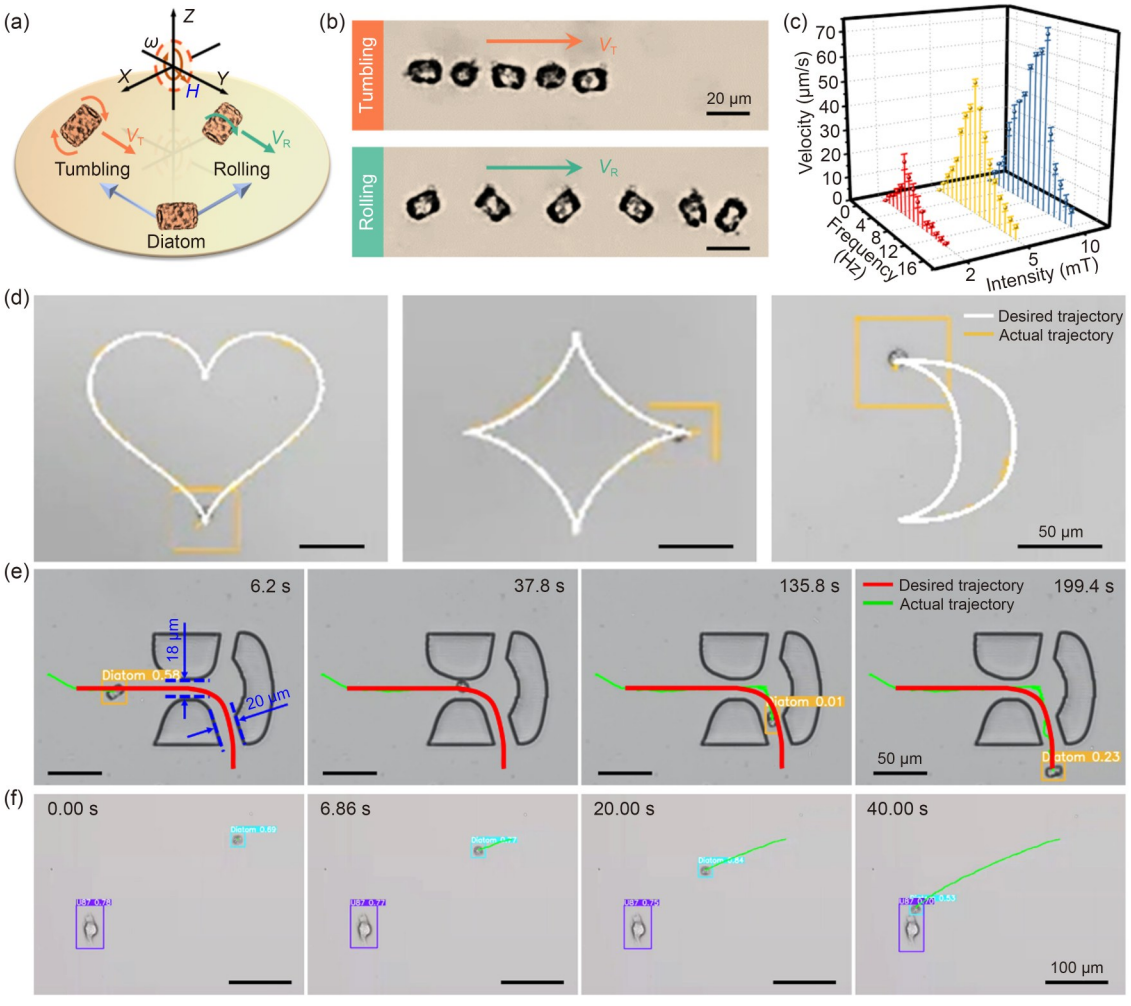


**Fig. 3** Locomotion of Mag-Diatoms. (a) Schematic illustration of Mag-Diatom rolling and tumbling modes. (b) Overlay snapshots showing two distinct motion modes of Mag-Diatoms. (c) Movement velocity of Mag-Diatoms under different magnetic field frequencies and intensities. (d) Trajectory tracking of Mag-Diatoms, with the yellow line representing the actual trajectory and the white line representing the desired trajectory. (e) Time-lapse images of a Mag-Diatom passing through a slit autonomously; the green line shows the actual trajectory and the red line shows the desired trajectory. (f) Time-lapse images of a Mag-Diatom autonomously navigating to the location of U87 cells

their initial position to the target position where U87 was located (Video S4 in the supplementary information). The algorithm defined an allowable error radius of 70 pixels (approximately 22.4 μm, with the center of the target cell as the reference point) for successful targeting. Considering that a U87 cell has an approximate length of 55 μm, reaching within this radius was regarded as successful completion of the targeted delivery task. Figure 3f shows the trajectory of a Mag-Diatom reaching the target U87 cell. At this point, the strength of the rotating magnetic field was 5 mT, with a frequency of 2 Hz. The straight-line distance between the Mag-Diatom and the U87 cell was 275.1 μm, and the Mag-Diatom required 40 s to reach the target. The success rate of the Mag-Diatom in targeting target cells was 88.89%. Failure primarily occurred when Mag-Diatoms adhered to the substrate and were immobilized, or when multiple Mag-Diatoms were simultaneously identified within the working area, preventing the algorithm from assigning the correct Mag-Diatom for control.

In summary, the PID controller enabled autonomous closed-loop motion control of the Mag-Diatoms, allowing them to autonomously change their motion modes to traverse narrow channels and thereby enhancing their environmental adaptability. Moreover, AI algorithms facilitated the detection of Mag-Diatoms and cells, autonomous trajectory planning, and targeted navigation of Mag-Diatoms along a predefined path to U87 cells.

## 3.3 PDT effect of Mag-Diatoms on U87 cells

To explore the PDT effect of chlorophyll in Mag-Diatoms on GBM, their in vitro cytotoxicity was first assessed using U87 cells. An overview of the experimental design is shown in Fig. 4a. Given that biocompatibility is essential

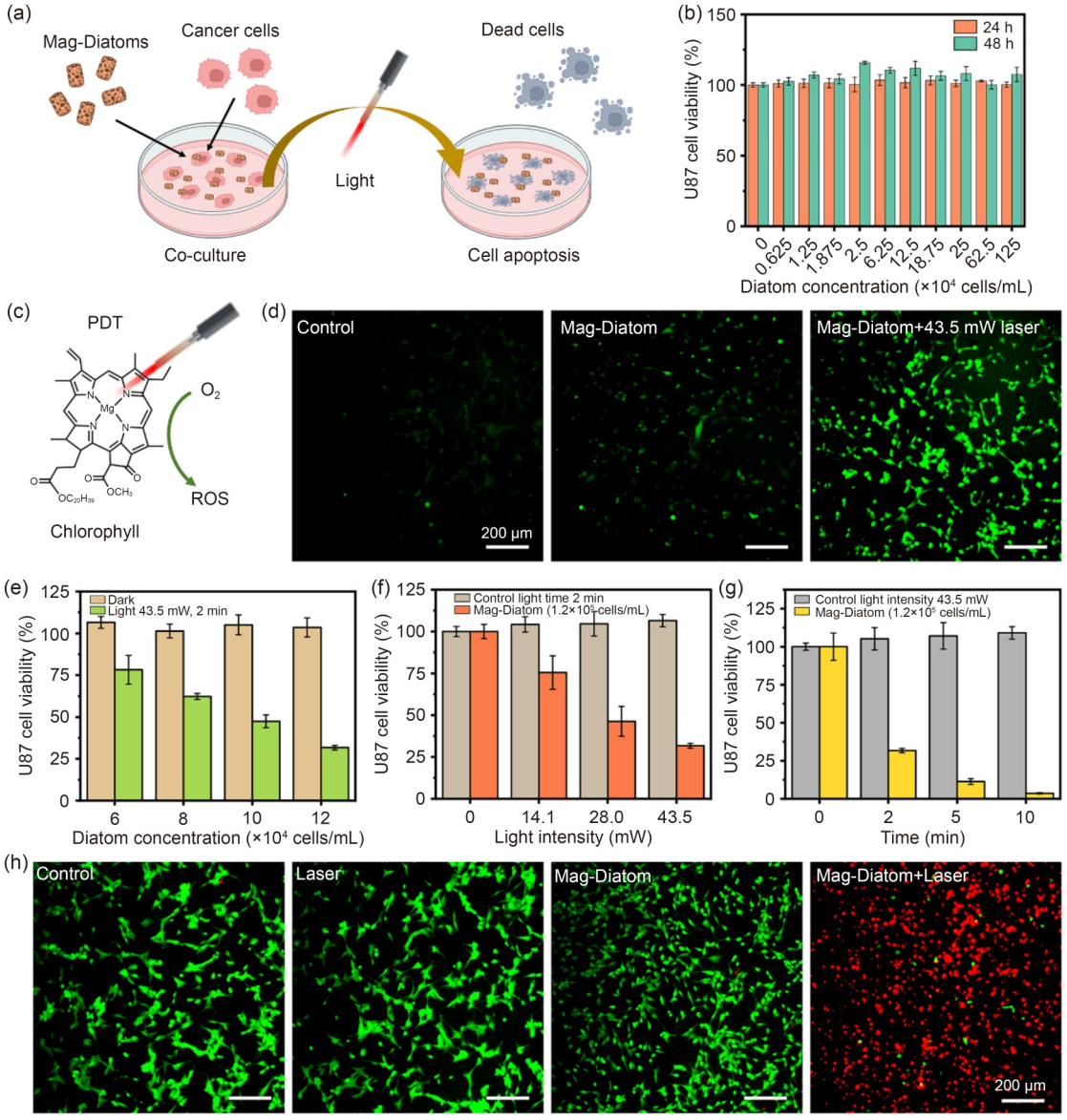


**Fig. 4** PDT effect of Mag-Diatoms on U87 cells. (a) Schematic illustration of the mechanism by which Mag-Diatoms act on tumor cells under laser irradiation. (b) Viability of U87 cells co-cultured with various concentrations of Mag-Diatoms for 24 or 48 h. (c) Schematic diagram showing chlorophyll-mediated ROS generation under laser irradiation for PDT. (d) Fluorescence images of U87 cells stained with DCFH-DA after different treatments. (e) Viability of U87 cells co-cultured with different concentrations of Mag-Diatoms and irradiated with or without a 43.5-mW laser for 2 min. (f) Viability of U87 cells co-cultured with or without Mag-Diatoms after 2 min of exposure to different laser intensities. (g) Viability of U87 cells co-cultured with or without Mag-Diatoms and exposed to a 43.5-mW laser for different durations. (h) Live/Dead fluorescence staining images of U87 cells after different treatments. Data in (b, e–g) are expressed as mean±standard deviation ($n$=3)

for biohybrid microrobots intended for targeted delivery, Mag-Diatoms were co-cultured with U87 cells and mouse hippocampal neuronal cells (HT22) for 24 or 48 h. The findings demonstrated that, within the tested concentration range (0–1.25×$10^6$ cells/mL), Mag-Diatoms caused almost no damage to U87 cells (Fig. 4b) or HT22 cells (Fig. S7 in the supplementary information). As a photosensitizer, chlorophyll can generate ROS under laser irradiation, thus achieving ROS-mediated PDT [59, 65–68] (Fig. 4c). To detect ROS generation, U87 cells co-cultured with Mag-Diatoms were stained with 2′,7-dichlorodihydrofluorescein diacetate (DCFH-DA). As shown in Fig. 4d, no green fluorescence was observed in U87 cells without laser irradiation, whereas green fluorescence was observed after laser irradiation, confirming the generation of ROS. Moreover, the ROS generation in U87 cells was examined at different light intensities (0, 14.1, 28.0, and 43.5 mW) (Fig. S8 in the supplementary information). As the laser intensity increased, the green fluorescence intensity observed in U87 cells also gradually increased. These results indicated that more and more ROS were produced, which proved that the chlorophyll in Mag-Diatoms had a good PDT effect. To

further evaluate the PDT efficacy, U87 cell viability was assessed using a standard CCK-8 cell assay. First, the effect of Mag-Diatom concentration on U87 cell viability under laser irradiation was tested (Fig. 4e). The results revealed that U87 cell viability decreased in a concentration-dependent manner, indicating greater cytotoxicity at higher Mag-Diatom concentrations. Moreover, exposure to varying light intensities (14.1, 28.0, and 43.5 mW) and irradiation times (2, 5, and 10 min) revealed that laser exposure alone caused minimal damage to U87 cells (Figs. 4f and 4g). However, the viability of U87 cells co-cultured with Mag-Diatom decreased to varying degrees under irradiation with different light intensities and laser durations. With increasing laser duration and light intensity, the cytotoxicity of Mag-Diatoms to U87 cells gradually increased. When the Mag-Diatom concentration was $1.2\times10^5$ cells/mL and irradiated with a 43.5-mW laser for 10 min, cell viability decreased to 3.6%. To further confirm these findings, calcein acetoxymethyl ester (calcein-AM)/propidium iodide staining was performed. While propidium iodide can only enter dead cells and operate on the cell nucleus, emitting red fluorescence, calcein-AM can pass through living cell membranes and produce green fluorescence. As shown in Fig. 4h, the control and Mag-Diatom groups emitted bright green fluorescence, indicating that the U87 cells had good viability. Conversely, the combination of Mag-Diatoms and laser light resulted in bright red fluorescence, indicating extensive cell death. These findings indicate that Mag-Diatom-mediated PDT has good cytotoxicity to U87 cells. This cytotoxic effect is strongly dependent on Mag-Diatom concentration, light intensity, and laser duration.

### 3.4 PDT effect of Mag-Diatoms on primary cells

To further examine the utility of Mag-Diatoms in tumor therapy and provide a reliable guidance for the clinical treatment of GBM, GSC63 cells isolated during the neurosurgical resection were used to evaluate the PDT effect of Mag-Diatoms. Figure 5a presents the isolation protocol for GSC63 cells. The primary cells, which exhibited optimal activity, appeared spherical and were cultured in suspension in serum-free medium. Bright-field and pseudo-colored SEM images of GSC63 under various experimental settings are displayed in Figs. 5b and 5c, respectively. In the SEM pseudo-colored images, GSC63 cells are shown in purple, and the Mag-Diatoms are shown in orange. The results indicated that GSC63 cells maintained their spherical morphology after co-culturing with Mag-Diatoms, with no remarkable morphological changes. However, upon laser irradiation, GSC63 cells co-cultured with Mag-Diatoms lost their spherical shape and spread out, indicating cell death. These experimental results suggest that Mag-Diatoms have a PDT effect on GSC63 cells. Subsequently, similar to U87 cells, the relationship between the PDT effect of Mag-Diatoms on GSC63 cells and the concentration of Mag-Diatoms (Fig. 5d), light intensity (Fig. 5e), and laser duration (Fig. 5f) was explored. The results showed that Mag-Diatoms exhibited minimal toxicity toward GSC63 cells in the absence of laser irradiation. Additionally, within the tested ranges of light intensities and irradiation durations, laser exposure alone did not affect GSC63 cell viability. However, cell viability decreased remarkably when GSC63 cells were exposed to both Mag-Diatoms and laser irradiation. When the Mag-Diatom concentration was $1.0\times10^5$ cells/mL and cells were irradiated with a 43.5-mW laser for 10 min, viability decreased to 19.5%. Moreover, the cytotoxicity effect of Mag-Diatoms on GSC63 cells increased with higher concentrations of Mag-Diatoms, greater light intensities, and longer irradiation durations. In conclusion, the prepared Mag-Diatoms exhibited strong PDT effects on GSC63 cells.

### 3.5 PDT effect of Mag-Diatoms in vivo

To evaluate the inhibitory effect of Mag-Diatoms on GBM in vivo, we established a mouse GBM model induced using SB mGSCs. Mice bearing orthotopic gliomas were implanted intracranially with Mag-Diatoms and treated with localized laser irradiation. Tumor progression was assessed by measuring fluorescence intensity through in vivo imaging, and body weight was recorded throughout the experiment (Fig. 6a).

Statistical analysis was performed using two-way analysis of variance (ANOVA) with Tukey's multiple comparison test. On Day 14, no significant differences in tumor fluorescence intensity were observed among the four groups. By Day 17, fluorescence intensity increased considerably in the Control, Laser, and Mag-Diatom groups, whereas the Mag-Diatom+Laser group exhibited a significant reduction ($p<0.001$). On Day 21, tumor fluorescence continued to rise in the Control, Laser, and Mag-Diatom groups, with no significant differences among them, while the Mag-Diatom+Laser group maintained a markedly lower signal ($p<0.001$) (Figs. 6b and 6c). These results demonstrate that neither laser irradiation alone nor Mag-Diatom alone inhibited tumor progression, but their combination remarkably suppressed GBM growth in vivo.

Body weight changes further supported these findings (Fig. 6d). From Day 14 to Day 22, progressive weight loss was observed in the Control, Laser, and Mag-Diatom groups, whereas mice in the Mag-Diatom+Laser group exhibited recovery, with statistically significant differences compared to the other groups.

On Day 22, the animals were euthanized, and their organs were collected for histological analysis. Hematoxylin and eosin (H&E) staining revealed no notable damage to

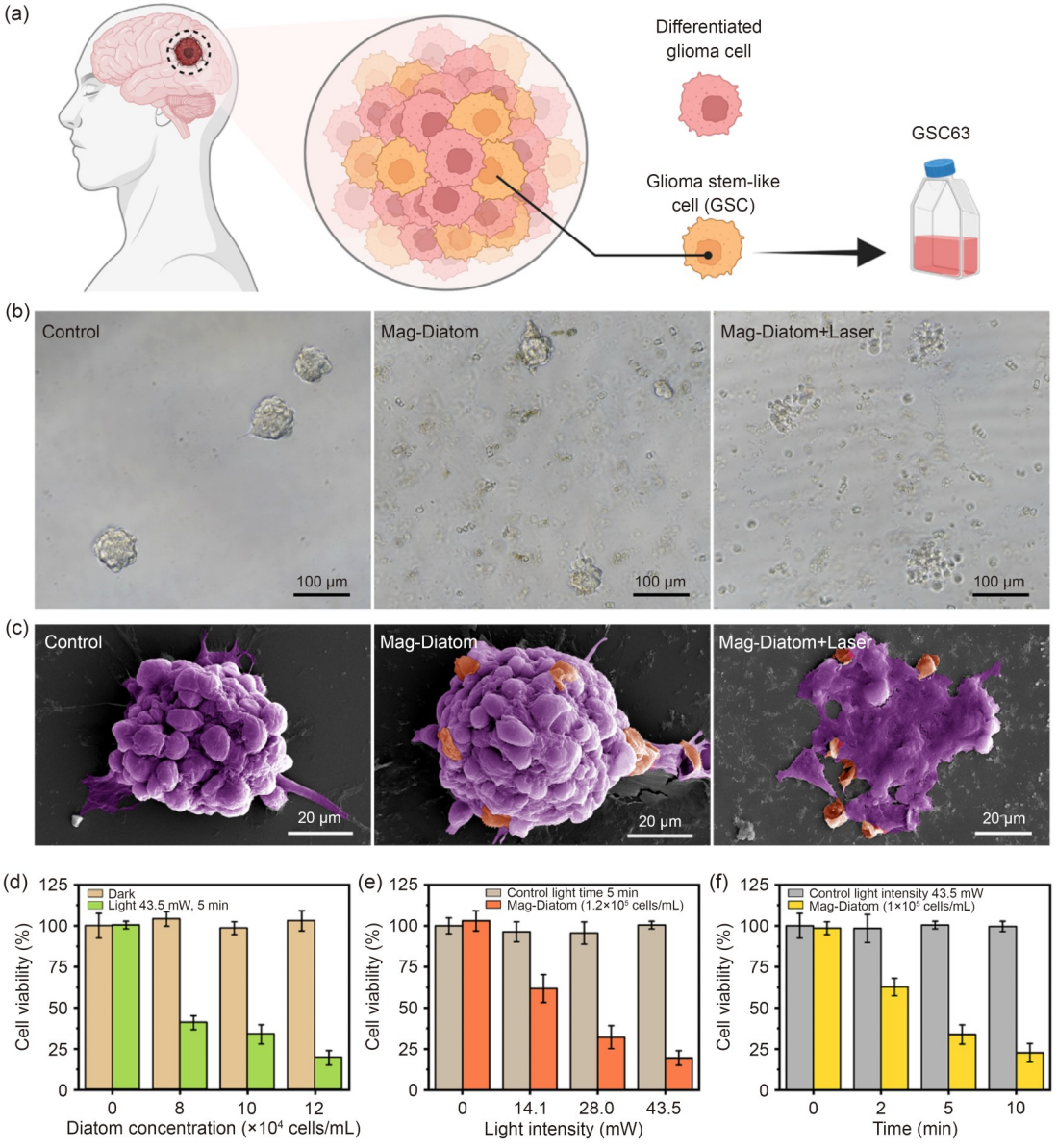


**Fig. 5** PDT effect of Mag-Diatoms on patient-derived primary cells. (a) Isolation protocol for glioma stem-like cells (GSC63): derived from surgically resected GBM tissue via enzymatic digestion, filtration, and serum-free culture. Bright-field images (b) and SEM pseudo-colored images (c) of GSC63 cells after different treatments. (d) GSC63 cell viability after co-culture with different concentrations of Mag-Diatoms and irradiation with or without the 43.5-mW laser for 5 min. (e) GSC63 cell viability after co-culture with or without the Mag-Diatoms after 5 min of exposure to different laser intensities. (f) GSC63 cell viability after co-culture with or without Mag-Diatoms after exposure to a 43.5-mW laser for different durations. Data in (d–f) are expressed as mean±standard deviation ($n$=3)

brain tissues or other major organs in any of the experimental groups compared with healthy controls (Fig. 6e). No evidence of hydropic degeneration or inflammatory infiltration was observed. Furthermore, immunohistochemical analysis of cluster of differentiation 68 (CD68) and tumor necrosis factor-alpha (TNF-α) expression across major organs showed no significant differences between the Control and Mag-Diatom+Laser groups (Fig. S9 in the supplementary information), supporting the favorable biosafety profile of this treatment and the absence of systemic immune activation. These findings indicate that Mag-Diatoms and the laser do not adversely affect the health of the mice.

## 4 Conclusions

In this study, we developed a novel diatom-based magnetic biohybrid microrobot—termed Mag-Diatom—derived from *T. weissflogii*, offering a biocompatible and scalable strategy for PDT of GBM. Notably, Mag-Diatoms harness the intrinsic chlorophyll of diatom cells as endogenous

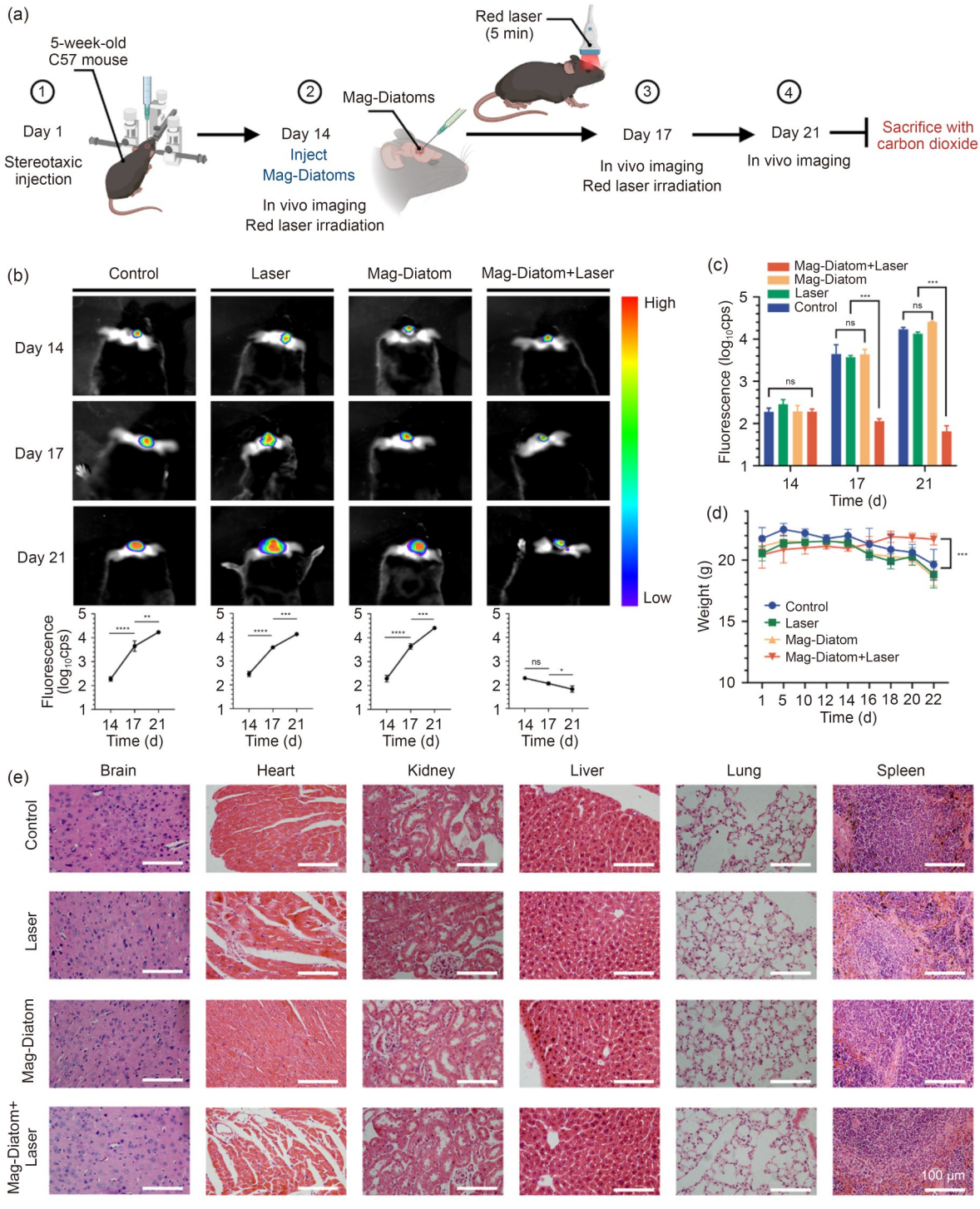


**Fig. 6** PDT effect of Mag-Diatoms in mouse models in vivo. (a) Flowchart illustrating the construction of the GBM mouse model and subsequent treatment protocol. (b, c) In vivo imaging on Days 14, 17, and 21 showing tumor luminescence intensity. Treatment groups: Control (no treatment), Laser (localized red laser irradiation), Mag-Diatom (intracranial injection of 1 μL Mag-Diatoms containing 25 000 units), and Mag-Diatom+Laser (intracranial injection of 1 μL Mag-Diatoms followed by localized red laser irradiation). (d) Body weights of mice subjected to various treatments from Days 1 to 22. (e) H&E staining of major organs harvested from treated mice. Data in (b–d) are expressed as mean±standard deviation ($n$=3). $^{*}p<0.05$, $^{**}p<0.01$, $^{***}p<0.001$, $^{****}p<0.0001$; ns: not significant

photosensitizers, eliminating the need for exogenous drug loading and thereby reducing the risk of drug leakage during targeted delivery. The Mag-Diatoms exhibited strong magnetic responsiveness and programmable motility, achieving a maximum velocity of 71.24 μm/s under a rotating magnetic field. Using PID-based control algorithms,

microrobots were capable of autonomous closed-loop trajectory tracking and successfully navigated through confined microenvironments by adaptively switching between dual motion modes. Furthermore, Mag-Diatoms exhibited precise targeting capabilities toward U87 cells under AI-guided navigation, laying a foundation for intelligent delivery systems. The PDT performance of Mag-Diatoms was comprehensively validated both in vitro and in vivo. Co-culture experiments with U87 GBM cell lines and patient-derived GSC63 confirmed that laser-activated Mag-Diatoms induced marked cytotoxicity, with therapeutic efficacy strongly dependent on laser intensity, irradiation duration, and microrobot concentration. Notably, following Mag-Diatom-mediated PDT, the viability of GSC63 dropped to 19.5%, compared with 3.6% observed in U87 cell lines. In a mouse glioma model, Mag-Diatom-mediated PDT remarkably suppressed tumor progression without inducing systemic toxicity or organ damage. Overall, Mag-Diatoms capitalize on the unique structural and biochemical properties of natural diatoms while integrating magnetic actuation and intelligent control. This platform represents a promising step forward in the development of minimally invasive, drug-free, and programmable microrobot systems for targeted cancer therapy, particularly for the treatment of GBM.

However, many challenges remain in bringing the results of this study into clinical application. First, the attenuation of magnetic fields by the skull may remarkably reduce navigation efficiency, thereby imposing higher requirements on both the magnetic control system and the locomotion performance of microrobots. Moreover, in vivo imaging of Mag-Diatoms needs to be further developed and optimized to improve the precision of targeted delivery. Currently, our research team is establishing large-animal glioma models to systematically evaluate their practical performance in clinically relevant scenarios, with a focus on overcoming key technical bottlenecks such as magnetic field penetration and real-time imaging navigation. Second, the limited penetration depth of light remains a critical issue for intracranial PDT, highlighting the need to optimize intracranial light delivery strategies and expand the therapeutic window of photosensitizers. Finally, the biodegradation and retrieval of Mag-Diatoms in vivo also require careful consideration, which may be addressed by designing degradable structures or combining cross-scale catheter-based delivery with subsequent retrieval strategies.

At the same time, to further improve the treatment efficacy of glioma and promote clinical translation, this research protocol can be combined with existing surgical methods or techniques. For example, coupling the Mag-Diatoms system with the Ommaya reservoir could enable repeated local intracranial administration via an implanted catheter. The incorporation of a rotating magnetic field generator and imaging modalities, such as ultrasound or fluorescence, into intraoperative navigation systems would improve microrobot positioning accuracy and mobility within the tumor microenvironment, thereby enhancing targeting efficiency. In terms of therapeutic strategies, multimodal synergy could be achieved: intraoperative magnetically guided PDT may eliminate residual tumor cells, followed by adjuvant temozolomide chemotherapy or radiotherapy to strengthen treatment outcomes. Furthermore, biocompatible diatom frustules can serve as drug carriers, enabling combined delivery of photosensitizers and chemotherapeutics. The Mag-Diatom delivery system, when combined with current glioma surgical platforms, holds much potential to enhance the targeted delivery potential of Mag-Diatoms and provide a novel technological paradigm for precise and scalable glioma treatment.

**Supplementary Information** The online version contains supplementary material available at https://doi.org/10.1631/bdm.2500276.

**Acknowledgements** This work was supported by the National Key R&D Program of China (No. 2023YFB4705600), the National Natural Science Foundation of China (Nos. U23A20342, U20A20380, 62273331, 62127811, and 82373342), CAS Project for Young Scientists in Basic Research (No. YSBR-036), New Cornerstone Science Foundation through the XPLORER PRIZE, CAS/SAFEA International Partnership Program for Creative Research Teams, the Science and Technology Planning Project of Liaoning Province (No. 2021JH1/10400049), Shengjing Hospital of China Medical University 345 Talent Project (No. 1000801592), the Joint Project of Liaoning Province (No. 2023JH2/101700202), and "the Fundamental Research Funds for the Central Universities", South-Central Minzu University (No. CZQ25014).

**Author contributions** All authors made significant contributions to this work. MYL, WC, and XCW contributed equally to the research design, data collection, and analysis. MYL and XCW drafted and revised the manuscript. JJZ, YTZ, and TYM participated in experimental execution and data analysis. AHW, LQL, and NDJ were responsible for research conceptualization, funding acquisition, supervision, and manuscript revision.

## Declarations

**Conflict of interest** The authors declare that they have no conflict of interest.

**Ethical approval** The experimental protocol was reviewed and approved by the Ethics Committee of Shengjing Hospital, China Medical University. All animal experiments adhered to the guidelines of the China Medical University Animal Care and Use Committee and were approved by the Institutional Review Board of Shengjing Hospital, China Medical University (approval number: 2023PS582K). Informed consent (both for participation and publication) was obtained from the patient, and the study protocol was approved by the Ethics Committee of the First Affiliated Hospital of China Medical University.

**Data availability** The data that support the findings of this study are available from the corresponding authors upon reasonable request.

**Use of generative AI tools** During the preparation of this work, the authors used AJE Curie service to improve language and readability,

and to check for grammatical errors. After using this tool, the authors reviewed and edited the content as needed and take full responsibility for the content of the publication.

## References


1. Lee J, Raj RR, Day NB et al (2023) Microrobots for biomedicine: unsolved challenges and opportunities for translation. *ACS Nano* 17(15):14196–14204. https://doi.org/10.1021/acsnano.3c03723
2. Yoo J, Tang SS, Gao W (2023) Micro- and nanorobots for biomedical applications in the brain. *Nat Rev Bioeng* 1(5): 308–310. https://doi.org/10.1038/s44222-023-00038-4
3. Li JX, de Ávila BEF, Gao W et al (2017) Micro/nanorobots for biomedicine: delivery, surgery, sensing, and detoxification. *Sci Robot* 2(4):eaam6431. https://doi.org/10.1126/scirobotics.aam6431
4. Nauber R, Goudu SR, Goeckenjan M et al (2023) Medical microrobots in reproductive medicine from the bench to the clinic. *Nat Commun* 14(1):728. https://doi.org/10.1038/s41467-023-36215-7
5. Schmidt CK, Medina-Sánchez M, Edmondson RJ et al (2020) Engineering microrobots for targeted cancer therapies from a medical perspective. *Nat Commun* 11(1):5618. https://doi.org/10.1038/s41467-020-19322-7
6. Gao CY, Wang Y, Ye ZH et al (2021) Biomedical micro-/nanomotors: from overcoming biological barriers to in vivo imaging. *Adv Mater* 33(6):2000512. https://doi.org/10.1002/adma.202000512
7. Sun TH, Chen JY, Zhang JY et al (2024) Application of micro/nanorobot in medicine. *Front Bioeng Biotechnol* 12:1347312. https://doi.org/10.3389/fbioe.2024.1347312
8. Sun BN, Kjelleberg S, Sung JJY et al (2024) Micro- and nanorobots for biofilm eradication. *Nat Rev Bioeng* 2(5):367–369. https://doi.org/10.1038/s44222-024-00176-3
9. Hu XY, Cheng W, Ma TY et al (2025) Bioinspired magnetic microspike robot for long-term drug delivery anchoring on gliomas. *Bio-Des Manuf* 8(4):558–569. https://doi.org/10.1631/bdm.2400508
10. Wang B, Kostarelos K, Nelson BJ et al (2021) Trends in micro-/nanorobotics: materials development, actuation, localization, and system integration for biomedical applications. *Adv Mater* 33(4):2002047. https://doi.org/10.1002/adma.202002047
11. Luo M, Feng YZ, Wang TW et al (2018) Micro-/nanorobots at work in active drug delivery. *Adv Funct Mater* 28(25):1706100. https://doi.org/10.1002/adfm.201706100
12. Fernández-Medina M, Ramos-Docampo MA, Hovorka O et al (2020) Recent advances in nano- and micromotors. *Adv Funct Mater* 30(12):1908283. https://doi.org/10.1002/adfm.201908283
13. Dutta S, Noh S, Gual RS et al (2023) Recent developments in metallic degradable micromotors for biomedical and environmental remediation applications. *Nano-Micro Lett* 16(1):41. https://doi.org/10.1007/s40820-023-01259-3
14. Tran HH, Watkins A, Oh MJ et al (2024) Targeting biofilm infections in humans using small scale robotics. *Trends Biotechnol* 42(4):479–495. https://doi.org/10.1016/j.tibtech.2023.10.004
15. Sun LY, Yu YR, Chen ZY et al (2020) Biohybrid robotics with living cell actuation. *Chem Soc Rev* 49(12):4043–4069. https://doi.org/10.1039/d0cs00120a
16. Murali N, Das SB, Yadav S et al (2024) Advanced biomimetic and biohybrid magnetic micro/nano-machines. *Adv Mater Technol* 9(19):2400239. https://doi.org/10.1002/admt.202400239
17. Shivalkar S, Chowdhary P, Afshan T et al (2023) Nanoengineering of biohybrid micro/nanobots for programmed biomedical applications. *Colloids Surf B Biointerfaces* 222:113054. https://doi.org/10.1016/j.colsurfb.2022.113054
18. Xu WX, Qin HF, Tian H et al (2022) Biohybrid micro/nanomotors for biomedical applications. *Appl Mater Today* 27:101482. https://doi.org/10.1016/j.apmt.2022.101482
19. Huang H, Lang YT, Wang SJ et al (2024) Microalgae-based drug delivery systems in biomedical applications. *Eng Regen* 5(3):361–374. https://doi.org/10.1016/j.engreg.2024.01.002
20. Zhang FY, Li ZX, Chen CR et al (2024) Biohybrid microalgae robots: design, fabrication, materials, and applications. *Adv Mater* 36(3):2303714. https://doi.org/10.1002/adma.202303714
21. Zhang FY, Guo ZY, Li ZX et al (2024) Biohybrid microrobots locally and actively deliver drug-loaded nanoparticles to inhibit the progression of lung metastasis. *Sci Adv* 10(24):eadn6157. https://doi.org/10.1126/sciadv.adn6157
22. Zhu SL, Cheng YF, Wang J et al (2023) Biohybrid magnetic microrobots: an intriguing and promising platform in biomedicine. *Acta Biomater* 169:88–106. https://doi.org/10.1016/j.actbio.2023.08.005
23. Nelson BJ, Kaliakatsos IK, Abbott JJ (2010) Microrobots for minimally invasive medicine. *Annu Rev Biomed Eng* 12:55–85. https://doi.org/10.1146/annurev-bioeng-010510-103409
24. Kankala RK, Han YH, Na J et al (2020) Nanoarchitectured structure and surface biofunctionality of mesoporous silica nanoparticles. *Adv Mater* 32(23):1907035. https://doi.org/10.1002/adma.201907035
25. Tang FQ, Li LL, Chen D (2012) Mesoporous silica nanoparticles: synthesis, biocompatibility and drug delivery. *Adv Mater* 24(12):1504–1534. https://doi.org/10.1002/adma.201104763
26. Niculescu VC (2020) Mesoporous silica nanoparticles for bioapplications. *Front Mater* 7:36. https://doi.org/10.3389/fmats.2020.00036
27. Xu C, Lei C, Yu CZ (2019) Mesoporous silica nanoparticles for protein protection and delivery. *Front Chem* 7:290. https://doi.org/10.3389/fchem.2019.00290
28. Maher S, Kumeria T, Aw MS et al (2018) Diatom silica for biomedical applications: recent progress and advances. *Adv Healthc Mater* 7(19):e1800552. https://doi.org/10.1002/adhm.201800552
29. Rogato A, De Tommasi E (2020) Physical, chemical, and genetic techniques for diatom frustule modification: applications in nanotechnology. *Appl Sci* 10(23):8738. https://doi.org/10.3390/app10238738
30. Sun XJ, Zhang MX, Liu JF et al (2024) The art of exploring diatom biosilica biomaterials: from biofabrication perspective. *Adv Sci* 11(6):2304695. https://doi.org/10.1002/advs.202304695
31. Min KH, Kim DH, Youn S et al (2024) Biomimetic diatom biosilica and its potential for biomedical applications and prospects: a review. *Int J Mol Sci* 25(4):2023. https://doi.org/10.3390/ijms25042023
32. Phogat S, Saxena A, Kapoor N et al (2021) Diatom mediated smart drug delivery system. *J Drug Deliv Sci Technol* 63: 102433. https://doi.org/10.1016/j.jddst.2021.102433
33. Khan MJ, Rai A, Ahirwar A et al (2021) Diatom microalgae as smart nanocontainers for biosensing wastewater pollutants:

recent trends and innovations. *Bioengineered* 12(2):9531–9549. https://doi.org/10.1080/21655979.2021.1996748
34. Deng YH, Ricciardulli T, Won J et al (2022) Self-locomotive, antimicrobial microrobot (SLAM) swarm for enhanced biofilm elimination. *Biomaterials* 287:121610. https://doi.org/10.1016/j.biomaterials.2022.121610
35. Seo Y, Leong J, Park JD et al (2018) Diatom microbubbler for active biofilm removal in confined spaces. *ACS Appl Mater Interfaces* 10(42):35685–35692. https://doi.org/10.1021/acsami.8b08643
36. Panda A, Reddy AS, Venkateswarlu S et al (2018) Bio-inspired self-propelled diatom micromotor by catalytic decomposition of $H_2O_2$ under low fuel concentration. *Nanoscale* 10(34): 16268–16277. https://doi.org/10.1039/C8NR04534H
37. Li MY, Wu JF, Lin DJ et al (2022) A diatom-based biohybrid microrobot with a high drug-loading capacity and pH-sensitive drug release for target therapy. *Acta Biomater* 154:443–453. https://doi.org/10.1016/j.actbio.2022.10.019
38. Yang CF, Feng C, Li YH et al (2023) Morphological and physicochemical characteristics, biological functions, and biomedical applications of diatom frustule. *Algal Res* 72:103104. https://doi.org/10.1016/j.algal.2023.103104
39. Abdul Rahman A, Mohd Isa IL, Tofail SAM et al (2024) Modification of living diatom, *Thalassiosira weissflogii*, with a calcium precursor through a calcium uptake mechanism: a next generation biomaterial for advanced delivery systems. *ACS Appl Bio Mater* 7(6):4102–4115. https://doi.org/10.1021/acsabm.4c00431
40. Saxena A, Dutta A, Kapoor N et al (2022) Envisaging marine diatom *Thalassiosira weissflogii* as a "SMART" drug delivery system for insoluble drugs. *J Drug Deliv Sci Technol* 68: 102983. https://doi.org/10.1016/j.jddst.2021.102983
41. Shergalis A, Bankhead A, Luesakul U et al (2018) Current challenges and opportunities in treating glioblastomas. *Pharmacol Rev* 70(3):412–445. https://doi.org/10.1124/pr.117.014944
42. Louis DN, Perry A, Wesseling P et al (2021) The 2021 WHO classification of tumors of the central nervous system: a summary. *Neuro Oncol* 23(8):1231–1251. https://doi.org/10.1093/neuonc/noab106
43. Bush NAO, Chang SM, Berger MS (2017) Current and future strategies for treatment of glioma. *Neurosurg Rev* 40(1):1–14. https://doi.org/10.1007/s10143-016-0709-8
44. Dea N, Fournier-Gosselin MP, Mathieu D et al (2012) Does extent of resection impact survival in patients bearing glioblastoma? *Can J Neurol Sci* 39(5):632–637. https://doi.org/10.1017/s0317167100015377
45. Chamberlain MC (2009) Bevacizumab for recurrent malignant gliomas: efficacy, toxicity, and patterns of recurrence. *Neurology* 72(8):772–773. https://doi.org/10.1212/01.wnl.0000339387.03225.0a
46. Yuan SX, Li JL, Xu XK et al (2018) Underlying mechanism of the photodynamic activity of hematoporphyrin-induced apoptosis in U87 glioma cells. *Int J Mol Med* 41(4):2288–2296. https://doi.org/10.3892/ijmm.2018.3400
47. Bhanja D, Wilding H, Baroz A et al (2023) Photodynamic therapy for glioblastoma: illuminating the path toward clinical applicability. *Cancers* 15(13):3427. https://doi.org/10.3390/cancers15133427
48. Cramer SW, Chen CC (2020) Photodynamic therapy for the treatment of glioblastoma. *Front Surg* 6:81. https://doi.org/10.3389/fsurg.2019.00081
49. Park J, Lee YK, Park IK et al (2021) Current limitations and recent progress in nanomedicine for clinically available photodynamic therapy. *Biomedicines* 9(1):85. https://doi.org/10.3390/biomedicines9010085
50. Tetard MC, Vermandel M, Mordon S et al (2014) Experimental use of photodynamic therapy in high grade gliomas: a review focused on 5-aminolevulinic acid. *Photodiagn Photodyn Ther* 11(3):319–330. https://doi.org/10.1016/j.pdpdt.2014.04.004
51. Falk-Mahapatra R, Gollnick SO (2020) Photodynamic therapy and immunity: an update. *Photochem Photobiol* 96(3):550–559. https://doi.org/10.1111/php.13253
52. Hwang HS, Shin H, Han J et al (2018) Combination of photodynamic therapy (PDT) and anti-tumor immunity in cancer therapy. *J Pharm Investig* 48(2):143–151. https://doi.org/10.1007/s40005-017-0377-x
53. Tsai YC, Vijayaraghavan P, Chiang WH et al (2018) Targeted delivery of functionalized upconversion nanoparticles for externally triggered photothermal/photodynamic therapies of brain glioblastoma. *Theranostics* 8(5):1435–1448. https://doi.org/10.7150/thno.22482
54. Wang XF, Tian Y, Liao X et al (2020) Enhancing selective photosensitizer accumulation and oxygen supply for high-efficacy photodynamic therapy toward glioma by 5-aminolevulinic acid loaded nanoplatform. *J Colloid Interface Sci* 565:483–493. https://doi.org/10.1016/j.jcis.2020.01.020
55. Wang Q, Li JM, Yu H et al (2018) Fluorinated polymeric micelles to overcome hypoxia and enhance photodynamic cancer therapy. *Biomater Sci* 6(11):3096–3107. https://doi.org/10.1039/c8bm00852c
56. Huang XQ, Wu JR, He MY et al (2019) Combined cancer chemo-photodynamic and photothermal therapy based on ICG/PDA/TPZ-loaded nanoparticles. *Mol Pharmaceutics* 16(5): 2172–2183. https://doi.org/10.1021/acs.molpharmaceut.9b00119
57. de Paula LB, Primo FL, Tedesco AC (2017) Nanomedicine associated with photodynamic therapy for glioblastoma treatment. *Biophys Rev* 9(5):761–773. https://doi.org/10.1007/s12551-017-0293-3
58. Qiao Y, Yang F, Xie TT et al (2020) Engineered algae: a novel oxygen-generating system for effective treatment of hypoxic cancer. *Sci Adv* 6(21):eaba5996. https://doi.org/10.1126/sciadv.aba5996
59. Zhong DN, Li WL, Qi YC et al (2020) Photosynthetic biohybrid nanoswimmers system to alleviate tumor hypoxia for FL/PA/MR imaging-guided enhanced radio-photodynamic synergetic therapy. *Adv Funct Mater* 30(17):1910395. https://doi.org/10.1002/adfm.201910395
60. Walter B, Peters J, van Beusekom JEE et al (2015) Interactive effects of temperature and light during deep convection: a case study on growth and condition of the diatom *Thalassiosira weissflogii*. *ICES J Mar Sci* 72(6):2061–2071. https://doi.org/10.1093/icesjms/fsu218
61. Wiesner SM, Decker SA, Larson JD et al (2009) *De novo* induction of genetically engineered brain tumors in mice using plasmid DNA. *Cancer Res* 69(2):431–439. https://doi.org/10.1158/0008-5472.CAN-08-1800
62. Zhong DN, Du Z, Zhou M (2021) Algae: a natural active material for biomedical applications. *VIEW* 2(4):20200189. https://doi.org/10.1002/VIW.20200189
63. Morozov KI, Leshansky AM (2014) The chiral magnetic nanomotors. *Nanoscale* 6(3):1580–1588. https://doi.org/10.1039/c3nr04853e
64. Li MY, Li L, Zhou JJ et al (2025) Deep learning-based automatic control of magnetic diatom biohybrid microrobots for targeted delivery. *IEEE Trans Robot* 41:2990–3003.

https://doi.org/10.1109/TRO.2025.3562452
65. Rizzi V, Fini P, Fanelli F et al (2016) Molecular interactions, characterization and photoactivity of Chlorophyll a/chitosan/2-HP-β-cyclodextrin composite films as functional and active surfaces for ROS production. *Food Hydrocoll* 58:98–112. https://doi.org/10.1016/j.foodhyd.2016.02.012
66. Sperandio FF, Huang YY, Hamblin MR (2013) Antimicrobial photodynamic therapy to kill Gram-negative bacteria. *Recent Pat Antiinfect Drug Discov* 8(2):108–120. https://doi.org/10.2174/1574891x113089990012
67. Song BH, Lee DH, Kim BC et al (2014) Photodynamic therapy using chlorophyll-a in the treatment of acne vulgaris: a randomized, single-blind, split-face study. *J Am Acad Dermatol* 71(4): 764–771. https://doi.org/10.1016/j.jaad.2014.05.047
68. Chu MQ, Li HK, Wu Q et al (2014) Pluronic-encapsulated natural chlorophyll nanocomposites for in vivo cancer imaging and photothermal/photodynamic therapies. *Biomaterials* 35(29): 8357–8373. https://doi.org/10.1016/j.biomaterials.2014.05.049